LEGIBILITY NOTICE

A major purpose of the Technical Information Center is to provide the broadest dissemination possible of information contained in DOE's Research and Development Reports to business, industry, the academic community, and federal, state and local governments.

Although a small portion of this report is not reproducible, it is being made available to expedite the availability of information on the research discussed herein.

LA-UR 89-2981

LA-UR--89-2981

DE89 016971

TITLE LOW-ENERGY PION DOUBLE CHARGE EXCHANGE AND NUCLEON-NUCLEON CORRELATIONS IN NUCLEI

AUTHOR(S) Michael J. Leitch

SUBMITTED TO Proceedings, Second LAMPF Workshop on Pion-Nucleus Double Charge Exchange, Los Alamos, NM, August 9-11, 1989

DISCLAIMER

Los Alamos Los Alamos National Laboratory
Los Alamos, New Mexico 87545

LOW-ENERGY PION DOUBLE CHARGE EXCHANGE AND NUCLEON-NUCLEON CORRELATIONS IN NUCLEI

MICHAEL J. LEITCH

Los Alamos National Laboratory

ABSTRACT

Recent measurements of pion double-charge exchange (DCX) at energies 20 to 70 MeV are providing a new means for studying nucleon-nucleon correlations in nuclei. At these energies the nucleus is relatively transparent, allowing simpler theoretical models to be used in interpreting the data and leading to a clearer picture. Also the contribution to DCX of sequential charge-exchange scattering through the intermediate analog state is suppressed near 50 MeV and transitions through non-analog intermediate states become very important. Recent theoretical studies by several groups have shown that while transitions through the analog route involve relatively long nucleon-nucleon distances, those through non-analog intermediate states obtain nearly half their strength from nucleon pairs with less than 1 fermi separation. Thus DCX near 50 MeV is an excellent way to study short-range nucleon-nucleon correlations.

I. WHY LOW ENERGY DCX?

Nuclei are relatively transparent to low-energy (20 to 80 MeV) pions and thus these pions penetrate nuclei much more than those with energies nearer the Δ_{33} resonance ($T_\pi \simeq 164$ MeV). This can be seen in Fig. 1 where I show data from the Tel Aviv group[1] for various components of the total $\pi - {}^{12}C$ cross section versus energy. If we concentrate on the total and the absorption cross sections we see that they both fall rapidly with decreasing energy below the resonance. This transparency near 50 MeV then allows simpler theoretical models (e.g., plane wave) to be applicable and helps to form a clearer picture for pion reactions in this energy range.

Of course this relative transparency also will exist well above the resonance, however, another very important feature of low-energy pions gives them a unique advantage. This feature can be seen in Fig. 2 which shows the zero-degree pion single-charge-exchange (SCX) cross sections for the proton ($\pi^- p \to \pi^0 n$) and for the isobaric-analog state (IAS) transition on various nuclei ($\pi^+ A \to \pi^- A'$). The sharp minimum for ${}^1H$ is due to a cancellation of the s- and p-wave amplitudes. What is somewhat surprising is that this

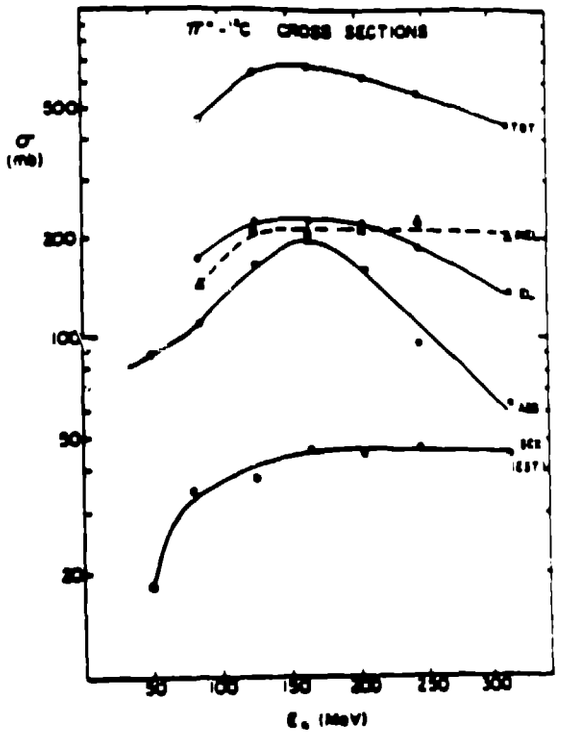

Fig. 1. Decomposition of the total π^+-carbon cross section. The lines are drawn to guide the eye. (Ref. 1.)

minimum persists for the IAS transition on nuclei up to ^{120}Sn. This both reaffirms the idea stated above that the nuclear medium effects on low-energy pion reactions are relatively weak and contributes an important feature to pion double-charge exchange reactions to the double-isobaric analog state (DIAS) near 50 MeV. Some other aspects of this interference minimum are shown in Figs. 3-5. In Fig. 3 we see the angular distributions for SCX to the IAS on ^{18}N over a broad range in energy. At 32 MeV the angular distribution is fairly flat but at 45 MeV we see the interference minimum which at 55 MeV has then move to an angle near 30°. Then at higher energies, nearer the Delta resonance, the angular distributions become diffractive. In Fig. 4 we see how the forward-angle minimum behaves with nuclear mass at a fixed energy. For the heavier nuclei it is less sharp. However this may be partially due to the fact that the energy at which the minimum is deepest changes with mass, as shown in Fig. 2. Finally, as shown in Fig. 5, even the angle-integrated IAS cross section shows a minimum near 50 MeV. We see that although at higher energies DCX via two forward-angle scatterings through an analog intermediate state (analog route) is allowed it is inhibited strongly near 50 MeV. Thus the analog route near 50 MeV is suppressed because it must go through large-angle scatterings and is missing the strength normally contributed by forward-angle scatterings. Then DCX routes through non-analog (NA) intermediate states become dominant and, as I will show below, these are much more interesting. These two types of routes, analog and NA, are schematically shown in Fig. 6.

Finally, we come to the unique properties of DCX. Since in a DCX reaction the pion must interact with two nucleons in the nucleus it is inherently sensitive to the correlations

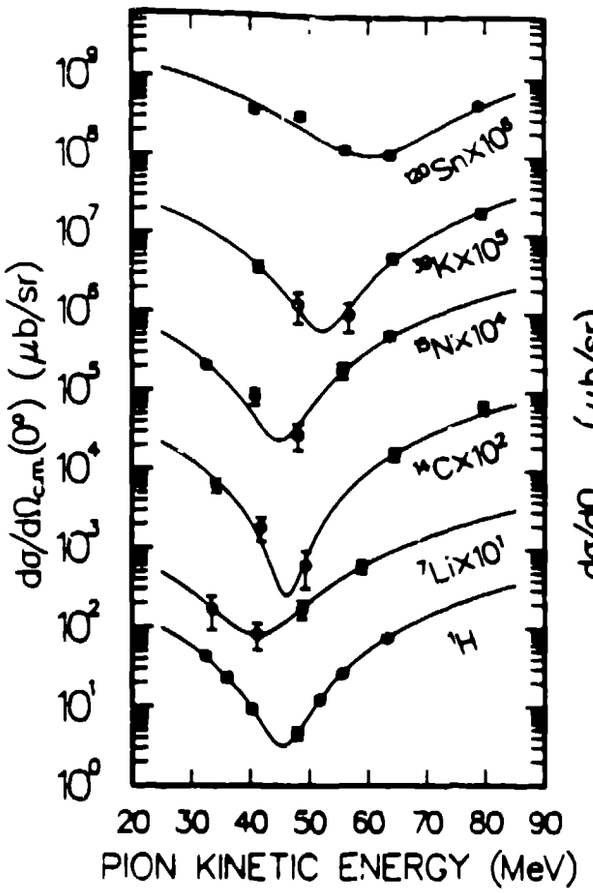

Fig. 2. Zero-degree SCX excitation functions for ^{1}H to ^{120}Sn (from Ref. 2) showing the persistance of the zero-degree minimum for SCX on nuclei. The lines are parabolic fits to the data.

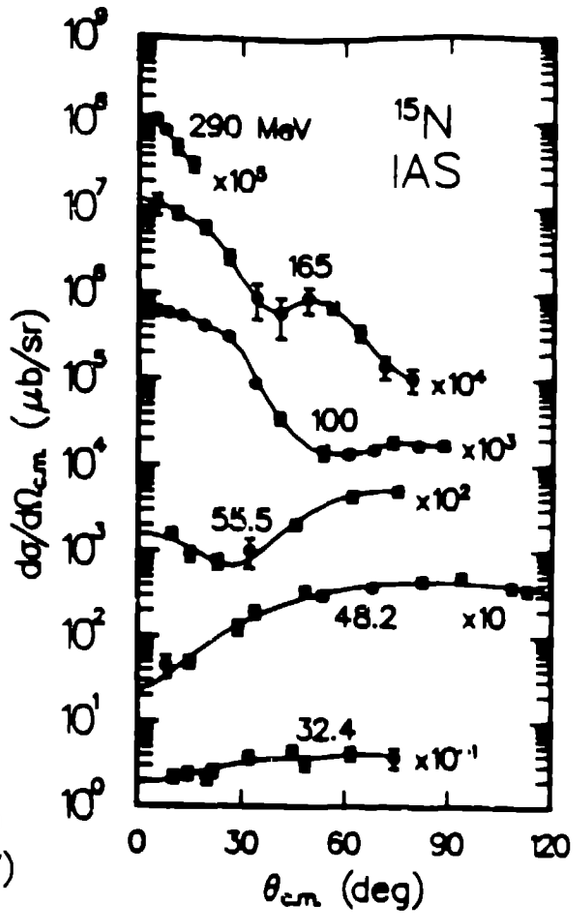

Fig. 3. Angular distributions for the $^{15}N(\pi^{+},\pi^{0})^{15}O(IAS)$ reaction over a broad range in energy. From Refs. 2-5.

of these nucleons. As we will see below, some of these correlations can be produced simply by the shell-model structure of their orbits. However, other more exotic "correlations" can come into the picture from mechanisms such as those depicted in Fig. 7. Mechanisms such as these are intrinsically very interesting and begin to bear on the question of the interface between quark and hadron degrees of freedom in the description of nuclei.

A final point about the relationship of SCX and DCX should be made. Any interpretation or calculation of DCX should also look at elastic scattering and SCX in a unified picture. A good illustration of this is provided by some old PIESDEX[9] calculations as shown in Fig. 8. Here we show two types of calculations with each done for both SCX and DCX. The dramatic feature is that although the two SCX calculations do not differ by a large amount the corresponding DCX calculations (analog-route only) differ by nearly

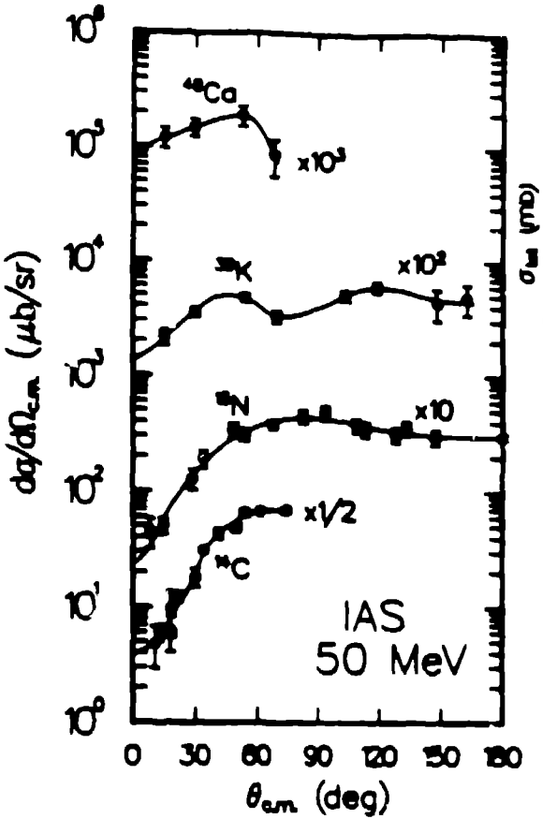

Fig. 4. Angular distributions for SCX to the IAS on several nuclei at 50 MeV. The data are from Refs. 3 and 6-7.

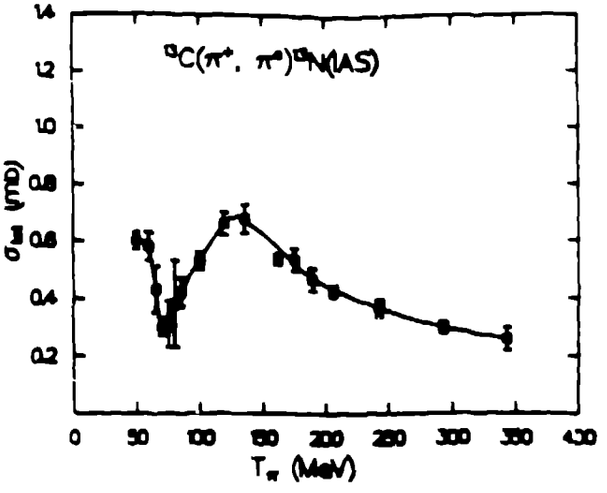

Fig. 5. Angle-integrated cross sections for the reaction $^{13}C(\pi^+, \pi^0)^{13}N(IAS)$ reaction as a function of energy obtained using activation techniques (Ref. 8).

an order of magnitude. Thus it is clear that SCX must be correctly described before a serious interpretation of DCX can be attempted.

II. UNEXPECTEDLY LARGE CROSS SECTIONS: ^{14}C AT 50 MeV

The first DCX experiments in the low-energy region were done at 50 MeV on ^{14}C at the TPIUMF/TPC[10] and shortly after with the Little Yellow Spectrometer (LYS) at LAMPF[11]. The energy resolution of the TPC experiment is just barely adequate to resolve the DIAS while that for the LAMPF experiment is $\sim 2\frac{1}{2}$ MeV. In Fig. 9 we see that the LAMPF data has much smaller uncertainties and extends all the way down to 20^0 scattering angle. The importance of small scattering angles is stressed by the theoretical calculations of Miller[12] which involve DCX directly on pre-existing 6-quark clusters. This speculation, which preceded the LAMPF measurements, caused considerable excitement at the time, however, since then more conventional models have also been able to describe the strong forward peaking in the angular distribution. As represented by the curve labeled "sequential optical model" simple calculations involving only the analog route produce small, flat cross sections. Δ-hole calculations of Karapiperis and Kobayashi[13] are shown

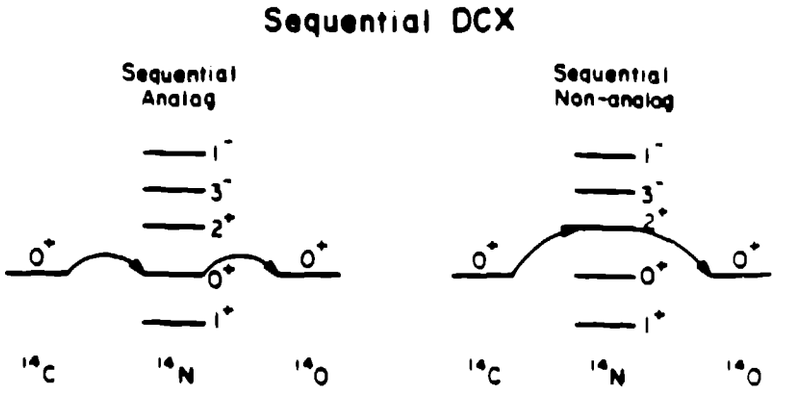

Fig. 6. Illustration of the two types of sequential scattering involved in DIAS transitions.

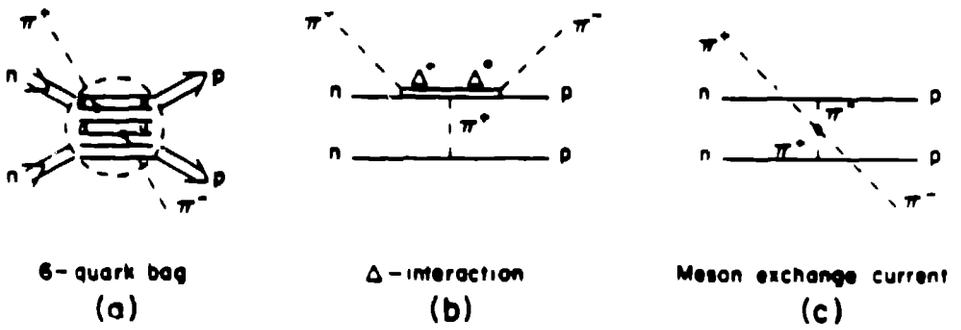

Fig. 7. Illustration of short-range DCX mechanisms.

in Fig. 10. The essential feature of these calculations is the inclusion of non-analog intermediate states, particularly the 2^+. Without this 2^+ intermediate state the cross section is small and flat. The multiple scattering calculations of Gibbs, Kaufmann, and Siegel[14] are shown in Fig. 11 and also include via closure the NA intermediate states. A very interesting feature of these calculations is that they are able to characterize the two-nucleon range and intermediate scattering angle of the process, as shown in Fig. 12. As discussed before, the process tends to involve two near 90° scatterings and also involves ranges less than 1 fm about 50% of the time. At this point one has to ask, with such short distances involved, is it still valid to think of the process in terms of nucleons? Thus, although the model involving quark degrees of freedom cannot be proved to be involved such effects may be hidden underneath a conventional approach.

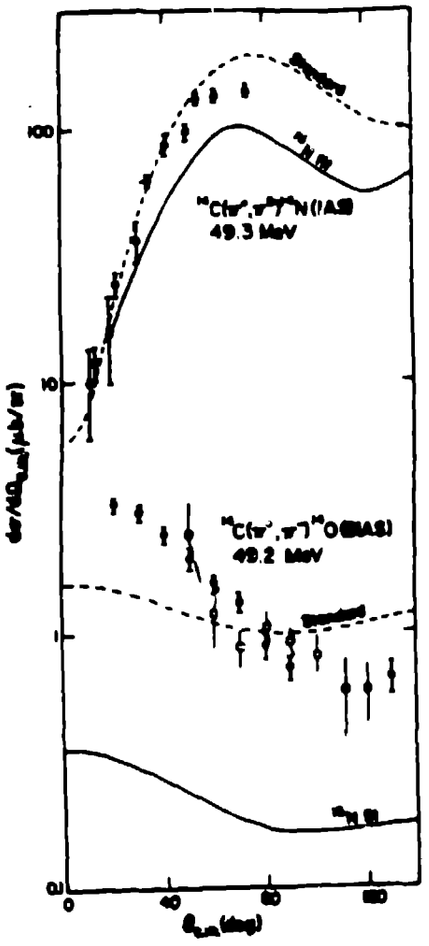

Fig. 8. PIESDEX calculations compared to SCX and DCX data as described in the text. The data is from Refs. 6, 10, and 11.

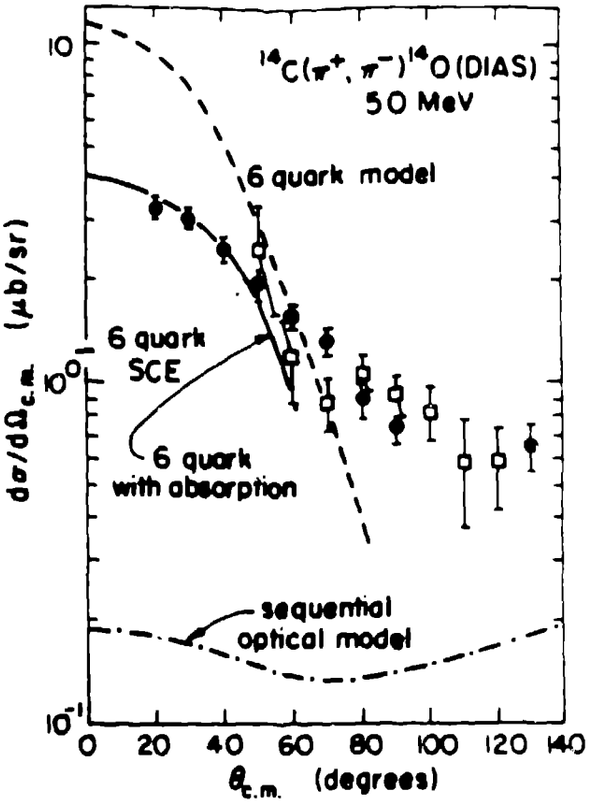

Fig. 9. $^{14}C(\pi^+,\pi^-)^{14}O$ (DIAS) at 50 MeV with Miller's 6-quark calculations[12]. The solid data points are the LAMPF data[11] and the open-squares are the TRIUMF data[10].

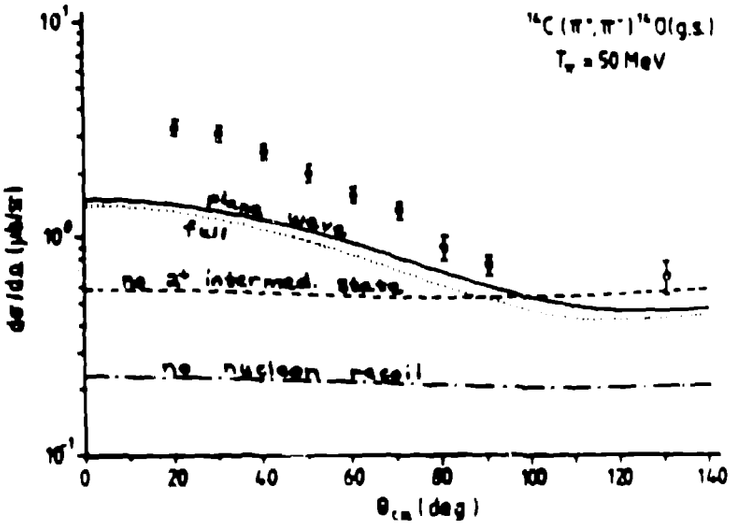

Fig. 10. Calculations of Karapiperis and Kobayashi from Ref. 13.

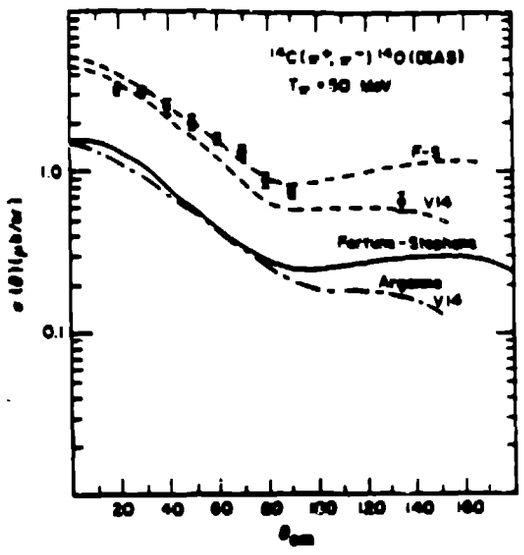

Fig. 11. DCX calculations of AGGK (Ref. 14) using various wave functions.

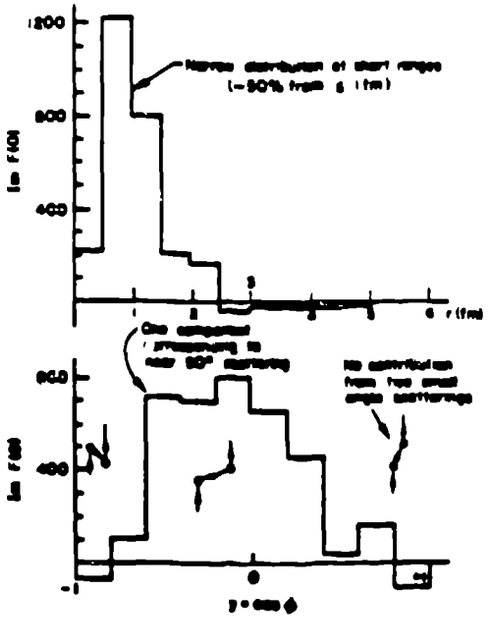

Fig. 12. At 50 MeV about half of the contributions to IM F(0) come from short distances ($\leq$ 1fm), and undergo two nearly 90° scatterings. (Ref. 6.)

Another approach has been used by Bleszynski and Glauber.[15] They have done plane-wave calculations with analog and NA intermediate states and with spin-flip in the closure approximation. As shown in Fig. 13 with Cohen-Kurath wave functions the agreement with the data is quite good. Also shown are curves for pure spin-singlet (^1S_o) and pure spin-triplet (^3P_o) states which have quite different angular distributions. As described in Ref. 13, this arises from the different correlation properties implicit in these two configurations. The ^3P_o wavefunction vanishes for $\vec{r}_1$ and $\vec{r}_2$ parallel or antiparallel while the ^1S_o is largest for these cases. Thus the ^1S_o doesn't inhibit $\vec{r}_1 \simeq \vec{r}_2$ for the two nucleons and will have more contributions from shorter-range N-N pairs. The angular distribution goes as the form factor of the centroid of the pair $\vec{R} = \frac{1}{2}(\vec{r}_1 + \vec{r}_2)$ which for a pair that has short range is $\vec{R} \sim \vec{r}_1 \sim \vec{r}_2$. Thus for a ^1S_o pair the centroid will extend to large radii corresponding to a sharply peaked form factor and producing a forward-peaked cross section. Their calculations also show (Fig. 14), as was discussed above, that NA intermediate states are essential to produce a forward-peaked cross section and also that including spin-flip reduces the forward-angle cross section by a substantial amount (~30%).

Following the measurements on ^{14}C additional 50 MeV angular distributions were measured by the TRIUMF group on the QQD magnetic spectrometer for ^{18}O and ^{26}Mg

(Refs. 16,17). As shown in Fig. 15 these cross sections are essentially identical in size and shape to those for ^{14}C. Thus the large forward-peaking feature is not nucleus specific and has no appreciable reduction with A for these T=1 nuclei.

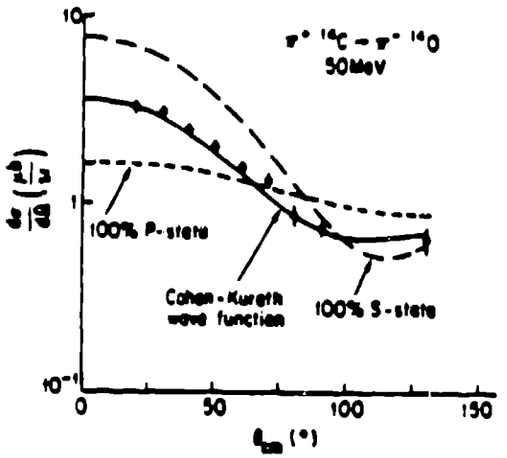

Fig. 13. Calculations of Bleszynski and Glauber (Ref. 15) using various configurations of the two ^{14}C valence neutrons (as labeled).

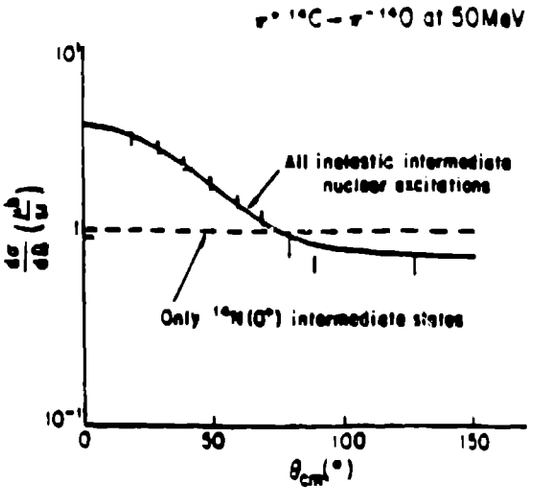

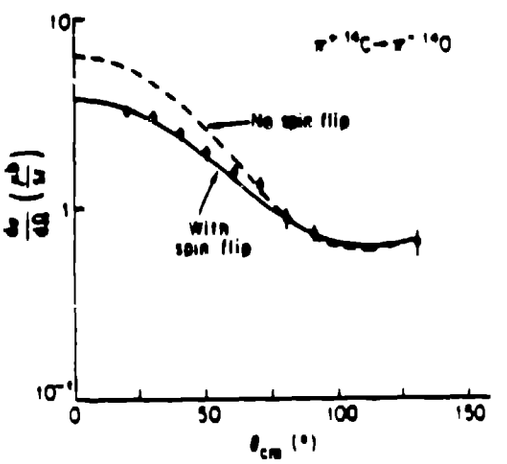

Fig. 14. Calculations of Bleszynski and Glauber (Ref. 15) showing the importance of NA intermediate states (top) and of spin-flip (bottom).

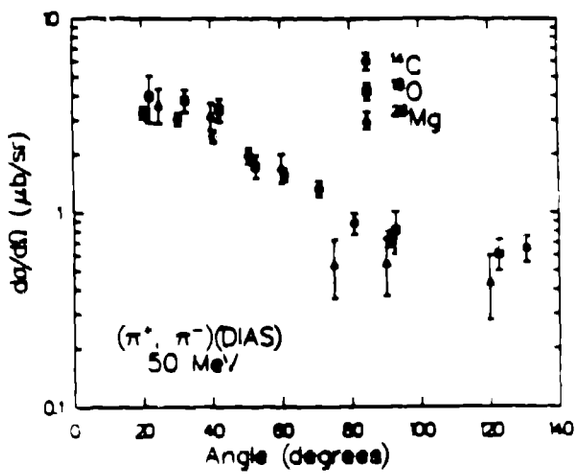

Fig. 15. Angular distributions at 50 MeV for ^{14}C, ^{18}O, and ^{26}Mg showing the nearly identical angular distributions (Refs. 11,16,17).

III. CLAMSHELL SPECTROMETER

For the experiments which followed (in 1986) a new magnetic spectrometer at LAMPF, the Clamshell spectrometer, has been used. This spectrometer, shown in Fig. 16, is a short (~2 meter average path length) magnetic spectrometer intended for low energy pions. Particle identification is obtained from the range of particles in the rear scintillators (S_2–S_7) and from the time-of-flight through the system (between S_1 and S_2).

In our most recent runs the Clamshell has been upgraded to include a forward-angle system which allows measurements of DCX at scattering angles as small as 10°. This is important, particularly at energies of 50 MeV and above, to give larger counting rates where the cross sections become increasingly forward peaked. Since typical measurements at one energy and angle take one to two days this system can make huge improvements in running times. The forward-angle setup is shown schematically in Fig. 17; it is similar to those used with other LAMPF spectrometers. A small sweep magnet just downstream of the experimental target bends the incident π^+ beam to the right while bending the π^- from DCX the opposite way into the spectrometer. For 0° scattering angle a separation

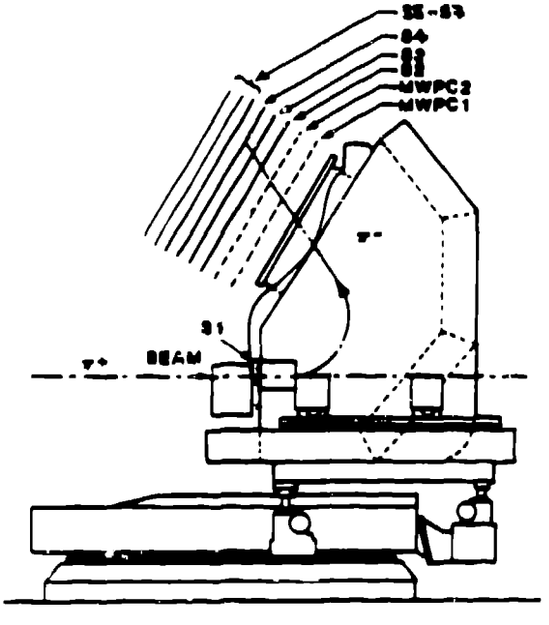

Fig. 16. Schematic diagram of the Clamshell Spectrometer system used for DCX measurements by our group at LAMPF.

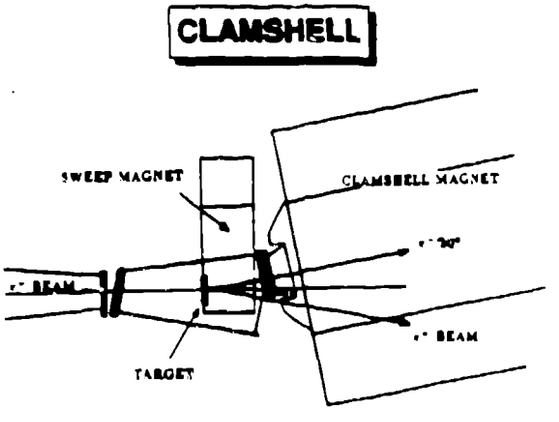

Fig. 17. Schematic of the forward-angle setup of the Clamshell.

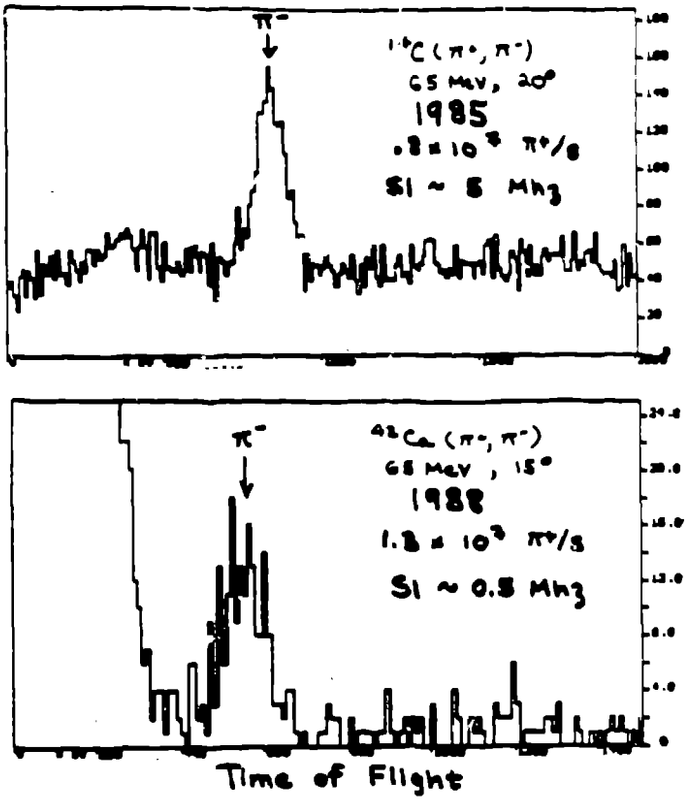

Fig. 18. A comparison of Clamshell time-of-flight spectra obtained with (top) and without (bottom) the forward-angle system under otherwise similar conditions. The large peak on the left of the top spectrum can be ignored. It is due to electron background and can easily be removed using pulse height cuts which have already been applied for the lower spectrum.

of approximately 20° (depending on reaction Q-value) between the π^+ and π^- results. With this system singles rates in the front scintillator (which usually limit the rate of beam on target) are almost an order of magnitude lower at a scattering angle of 15° now than they were before at 20°. A comparison of the time-of-flight spectra obtained for similar conditions with and without the forward angle system is shown in Fig. 18.

An even more significant advance is expected by 1990. This involves adding a superconducting RF cavity called the "scruncher" to the Low Energy Pion beam line which will compress the momentum spread of the incident beam allowing us to run with the full pion flux of the channel yet still obtain good resolution. We expect this will give approximately a factor of three higher counting rate and will also allow us to obtain 1 MeV (fwhm) resolution for all but the very low-energy measurements ($T_\pi \leq 25$ MeV) where target thickness effects dominate.

IV. 19–80 MEV ^{14}C

Some of the spectra obtained at energies 19 to 80 MeV for $^{14}C(\pi^+,\pi^-)$ are shown in Fig. 19. One remarkable feature is the rapid rise with energy in the non-analog strength at $E_x \geq 5$ MeV. The angular distributions for the DIAS transition are shown in Fig. 20. The shapes are flatter at low energy and steeper at higher energies, as one might expect. The

dramatic energy dependence of this ^{14}C data along with similar data for ^{12}C from Ref. 19 are shown in Fig. 21. Both the ^{14}C DIAS and the ^{12}C non-analog ground state transitions display similar behavior suggesting that the same mechanisms may be involved. It is also important to note that the ^{14}C data actually peaks near 50 MeV falling off rapidly on either side. Similar data for the ^{18}O DIAS taken later by the TRIUMF group[16,17] have the same feature.

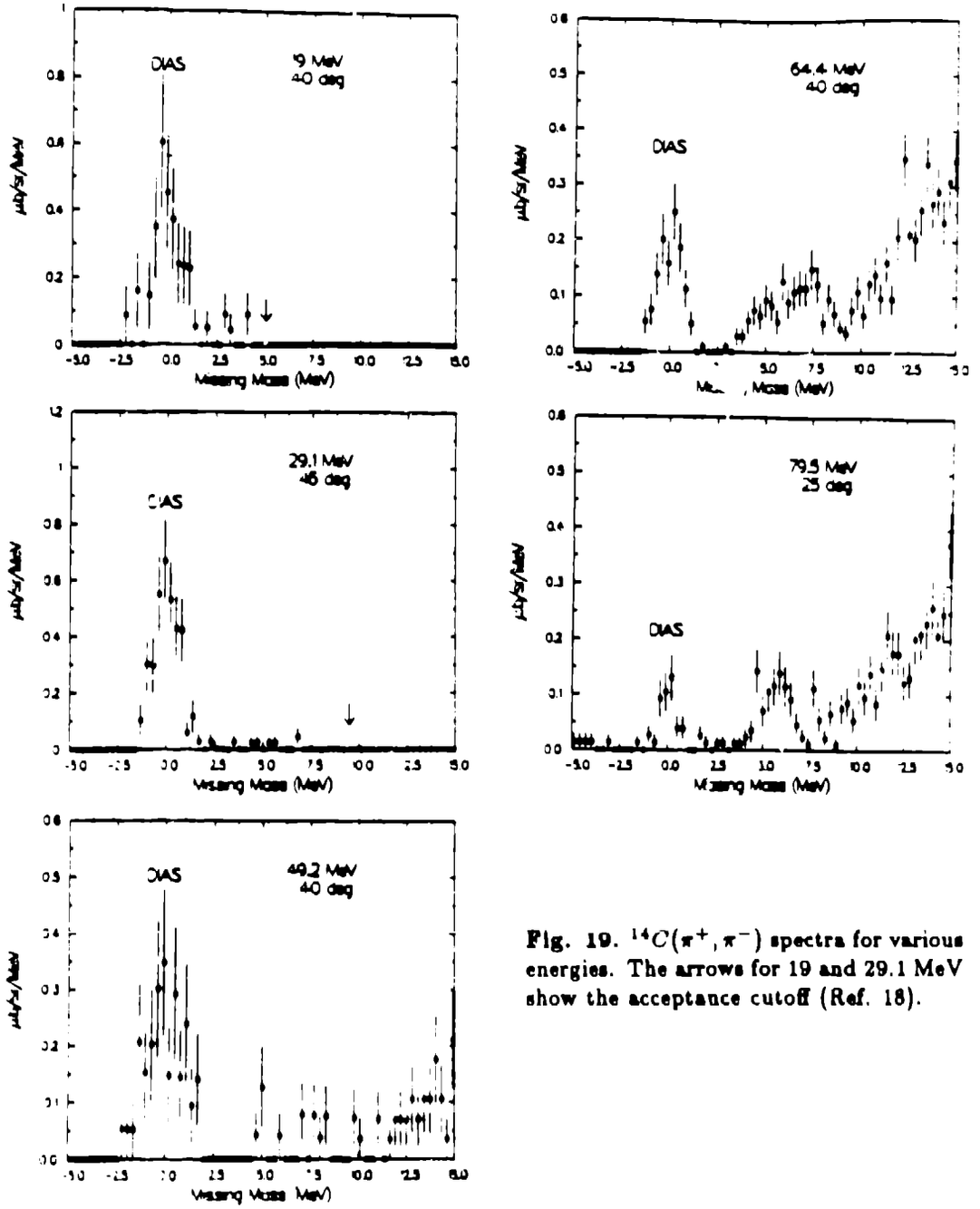

Fig. 19. $^{14}C(\pi^+,\pi^-)$ spectra for various energies. The arrows for 19 and 29.1 MeV show the acceptance cutoff (Ref. 18).

One of the problems which has surfaced in the theoretical interpretation of these data is the uncertainty of the pion absorption input used in DCX calculations. In Fig. 22 are shown calculations of Gibbs and Kaufmann based upon two contradictory sets of absorption data (see Refs. 1 and 23). It is clear that this discrepancy needs to be resolved, perhaps with new absorption data, in order to obtain a clear picture for DCX.

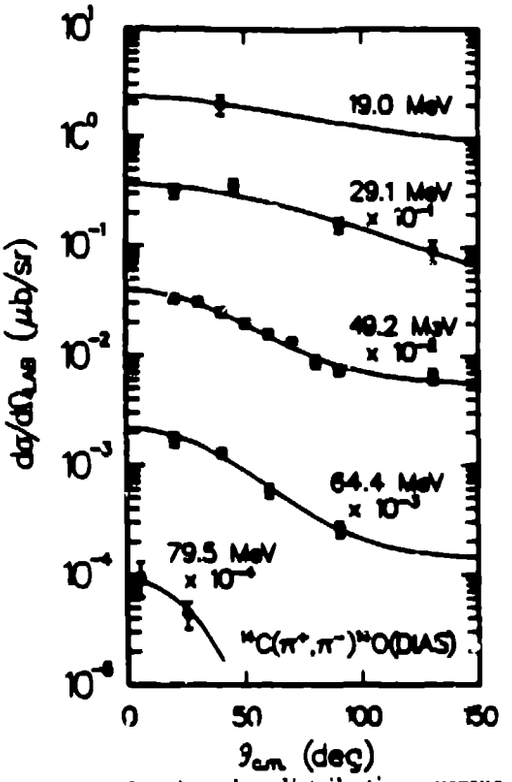

Fig. 20. Angular distributions versus energy for the $^{14}C(\pi^+,\pi^-)^{14}0$ (DIAS) reaction. The curves are to guide the eye.

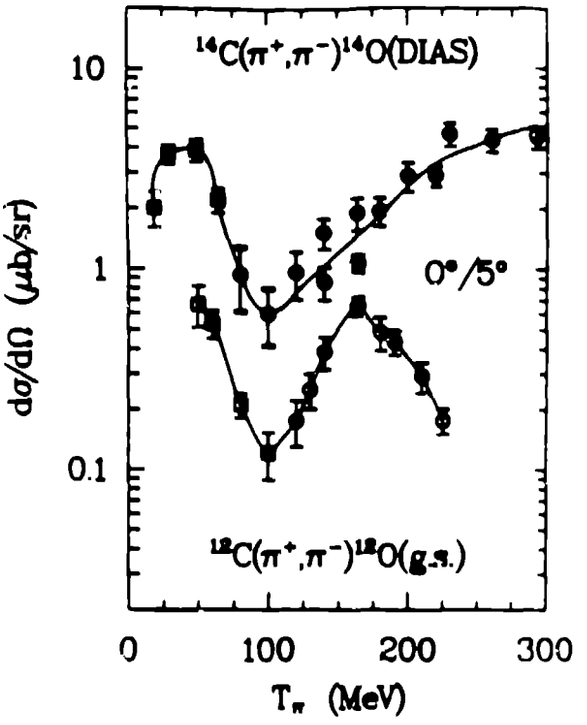

Fig. 21. The energy dependences of the 0/5° cross sections of DCX for the ^{14}C DIAS and ^{12}C g.s. transitions are very similar. Data is from Refs. 11, 18, 20, 21 (^{14}C) and Ref. 19. (^{12}C).

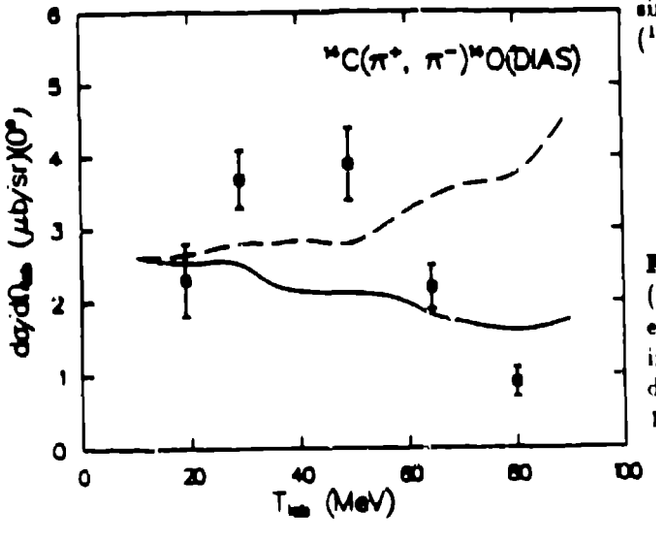

Fig. 22. Calculations of $^{14}C(\pi^+,\pi^-)^{14}0$ (DIAS) by AGGK (Ref. 22) for two different absorption strengths: solid curve using the data of Nakai *et al.* (Ref. 23) and dashed curve with the Tel Aviv data (Ref. 1). The DCX data is from Ref. 18.

V. ISOTOPIC COMPARISONS IN THE $f^{7/2}$ SHELL

After the measurements on light T = 1 nuclei our group began to look at the calcium isotopes. Initial attempts to measure ^{48}Ca at 50 MeV were unsuccessful because the DIAS lies at an excitation of 17.1 MeV amidst a very strong continuum (Fig. 23). However at 35 MeV, where the continuum strength is dramatically reduced the spectra shown in Fig. 24 were obtained (Refs. 24, 25). The cross sections obtained at a 40° scattering angle are shown in Table I along with a two-amplitude (AB) analysis following Auerbach, Gibbs, and Piasetzky.[26] First let us look at just the experimental numbers. Although ^{44}Ca has six times more neutron pairs for the DCX to take place on, the measured cross section is nearly a factor of two smaller than that of ^{42}Ca. Also, although ^{48}Ca has 28 times more pairs than ^{42}Ca, it is only slightly larger than ^{42}Ca. Clearly something unique and dramatic is happening near 50 MeV.

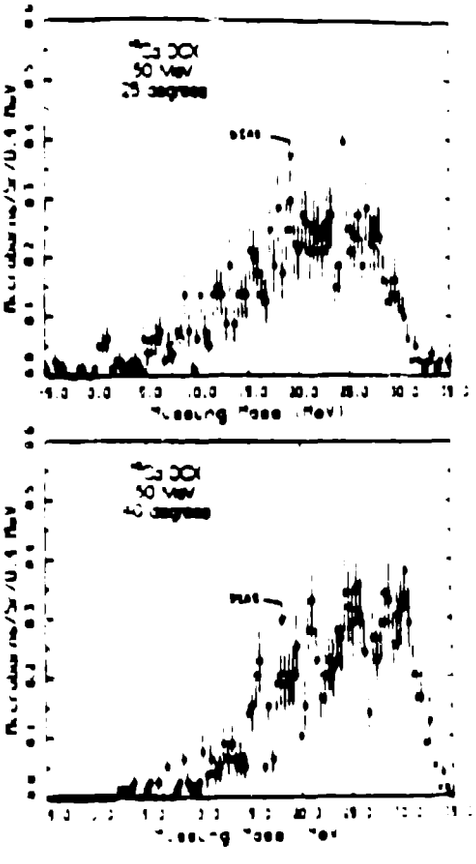

Fig. 23. Spectra for DCX on ^{48}Ca at 50 MeV where we were unable to observe the DIAS transition.

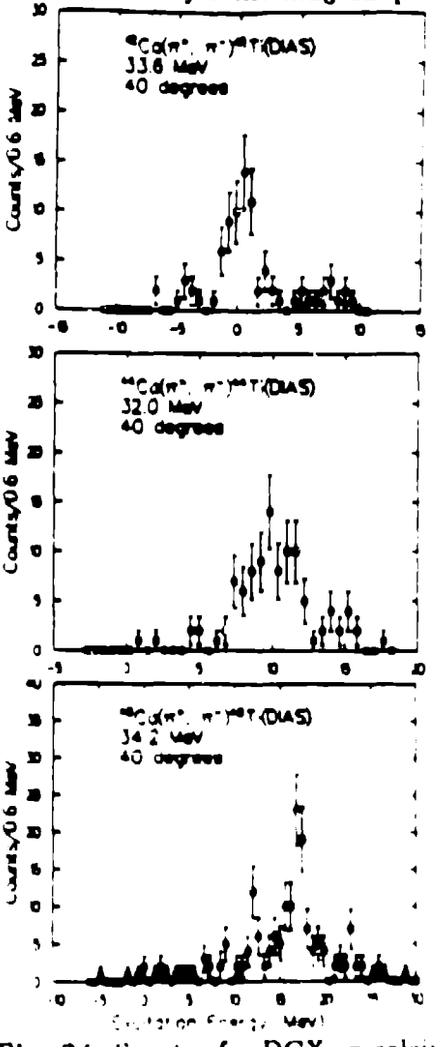

Fig. 24. Spectra for DCX on calcium isotopes at 35 MeV and 40° (Ref. 25)

Table I.

Phenomenological AB analysis of the 35 MeV, 40° Ca isotope data[19]

Target	AB Model	$d\sigma/d\Omega(35 NeV, 40°)(\mu b/sr)$
^{42}Ca	$\|A+B\|^2$	$2.0 \pm .5$
^{44}Ca	$\|A+\frac{1}{9}B\|^2$	$1.1 \pm .15$
^{48}Ca	$\|A-\frac{1}{7}B\|^2$	$2.4 \pm .6$

$$|A| = .34 \pm .03, \quad |B| = 1.20 \pm .14, \quad \phi = 59 \pm 12, \quad |\tfrac{B}{A}| = 3.5 \pm .5$$

Because of the shell-model configuration of the valence neutrons for each isotope, as shown in Ref. 27, transitions through non-analog states (B amplitude) are weighted by different factors relative to transitions through the analog route (A amplitude). In the seniority model the cross section goes as,

$$\frac{d\sigma^{DIAS}}{d\Omega}(\theta) = \frac{n(n-1)}{2}|A(\theta) + \frac{2j+3-2n}{(n-1)(2j-1)}B(\theta)|^2 \quad , \qquad (1)$$

where n is the number of valence neutrons, j is the orbital angular momentum (7/2 for the $f^{7/2}$-shell), and A and B are complex amplitudes representing transitions through analog and non-analog intermediate states, respectively. The factor $n(n-1)/2$ is the pair factor, i.e., the number of valence neutron pairs. The unique feature of low-energy is that A, the analog route, is suppressed near 50 MeV due to the s, p-wave cancellation in SCX. Thus as shown in some theoretical calculations of Auerbach, Gibbs, Ginocchio, and Kaufmann[27] (Fig. 25) the ratio $|B|/|A|$ becomes very large causing the shell-model variation between isotopes to produce huge differences in the cross sections. In Table I phenomological values for $|A|, |B|$ and the relative phase are extracted by fitting to the three data points and do give a large $|B|/|A|$ value of $3.5 \pm .5$. I will show below how this phenomological picture holds up for more than three data points (where it has predictive power) after I have introduced the newest data. So, in summary, since B is large compared to A the quantity inside the vertical bars is large for ^{42}Ca, but for ^{44}Ca and ^{48}Ca is so small (with the 1/9 + -1/7 factors) that even with the larger pair factors the resulting cross sections are similar to those for ^{42}Ca.

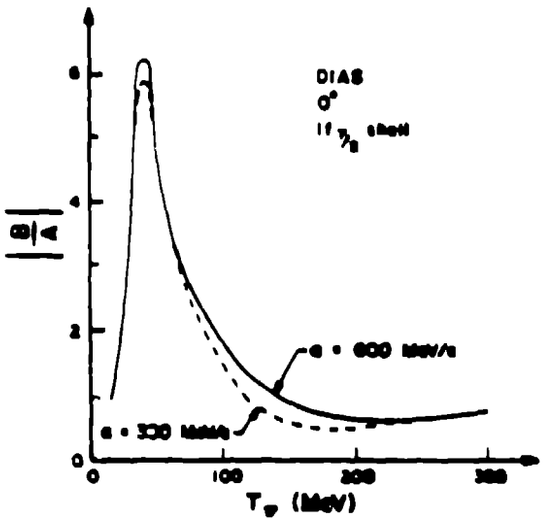

Fig. 25. Calculation of Ref. 27 showing the sharp peaking of $|B|/|A|$ near 50 MeV as described in the text.

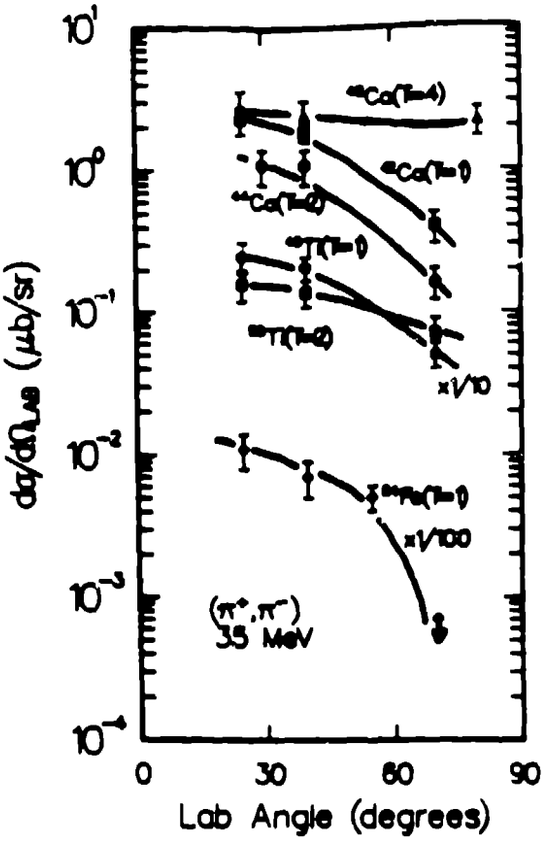

Fig. 26. Preliminary forward-angle distributions from our LAMPF experiment #1045 for DIAS transitions on several $f^{7/2}$-shell nuclei at 35 MeV (Refs. 24, 25, 28).

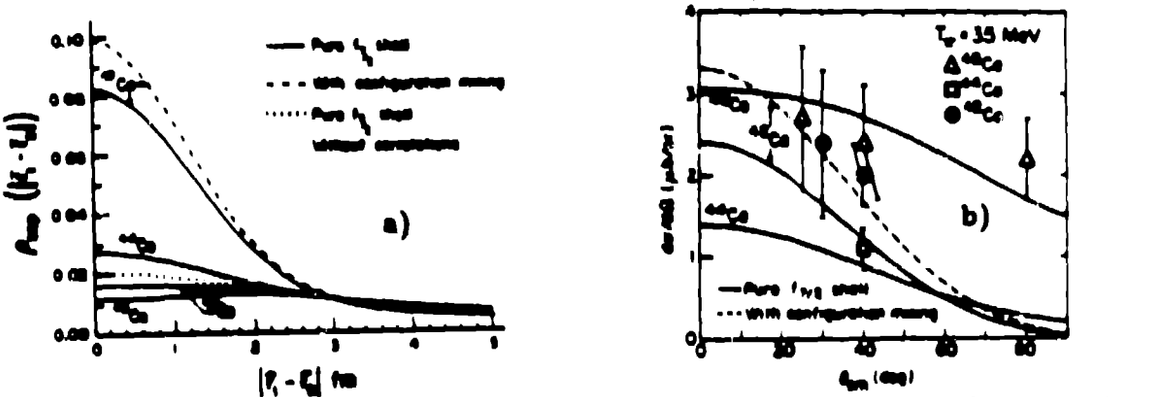

Fig. 27. From Blessynski, Blessynski, and Glauber (Ref. 33). a) The separation densities for ^{42}Ca, ^{44}Ca, ^{46}Ca, and ^{48}Ca (solid lines). The dotted curve is the separation density with the correlation function C_{N-s} set equal to zero. The dashed curve corresponds to a configuration-mixed representation of ^{42}Ca. b) Comparison between the theoretically predicted differential cross sections and the experimental data for the reactions $\pi^+ {}^A Ca(O^+) \rightarrow \pi^- {}^A Ti(O^+)$, for A = 42, 44, and 48, at 35 MeV.

Our newer (preliminary) data for a number of $f^{7/2}$ nuclei with 3-point angular distributions[24,25,28] is shown in Fig. 26. Of particular note is the difference in angular distribution shapes between $T = 1$ (steeper) and $T \geq 2$ (flatter) nuclei cross sections. These features have been explained by Bleszynski, Bleszynski, and Glauber (BBG).[29] Some BBG results are shown in Fig. 27. The N-N separation involved is strongly peaked at smaller range for ^{42}Ca which has the large contribution from the "B" term Thus the B term is strongly sensitive to the shorter-range correlations and thus is of particular interest. Also important to note is that a small amount configuration mixing from the $P_{3/2}$-shell substantially increases the forward-angle cross section. Clearly configuration mixing is an important ingredient of the full picture. The results shown here were also shown in a recent Physics Today article.[30] There is good agreement with the data and the more steeply falling cross section for ^{42}Ca (T=1) is also evident.

VI. ENERGY DEPENDENCE OF DIAS AND G.S. TRANSITIONS FOR $f^{7/2}$-SHELL NUCLEI

Our most recent data (July 1988) addresses the energy dependence of both DIAS and g.s. transitions on the $f^{7/2}$-shell nuclei. The new Clamshell forward-angle system (described above), which we developed along with MP-10, was used. Some of the spectra obtained are shown in Fig. 28. Some of these data are preliminary as they are from on-line analysis. They are summarized in Fig. 29 which shows the energy dependence including other data above 70 MeV from Kaletka[31] for perspective. Both DIAS and g.s. cross sections have huge rises at energies below 70 MeV. For ^{42}Ca a dramatic and rather sharp peak at 50 MeV is evident. Further data will be taken in 1989 to better define these features. At this time it is difficult to say what mechanisms cause such dramatic features but one can guess that since the features of the DIAS and g.s. transitions are similar a common source may be responsible. Also, since the Q-values involved, shown in Table II, vary dramatically this could account for the apparent energy-shifts between the peaking for some of the different transitions.

With this larger body of data, we can now take a more serious look at the phenomenological AB model. Note that the ground state transitons are also part of the AB picture and in fact have cross sections which go as $|B|^2$. Some of the nuclei (those with both valence neutrons and protons) do not follow the simple seniority shell-model picture of

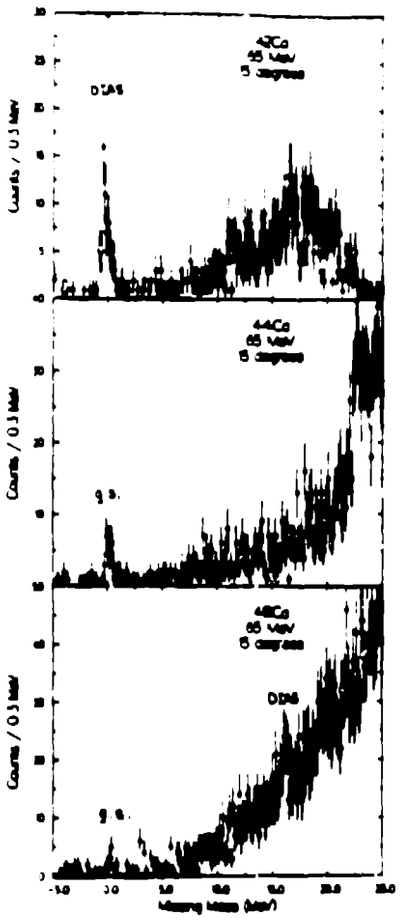

Fig. 28. Spectra from our LAMPF Exp. 1098 for 65 MeV DCX on calcium isotopes.

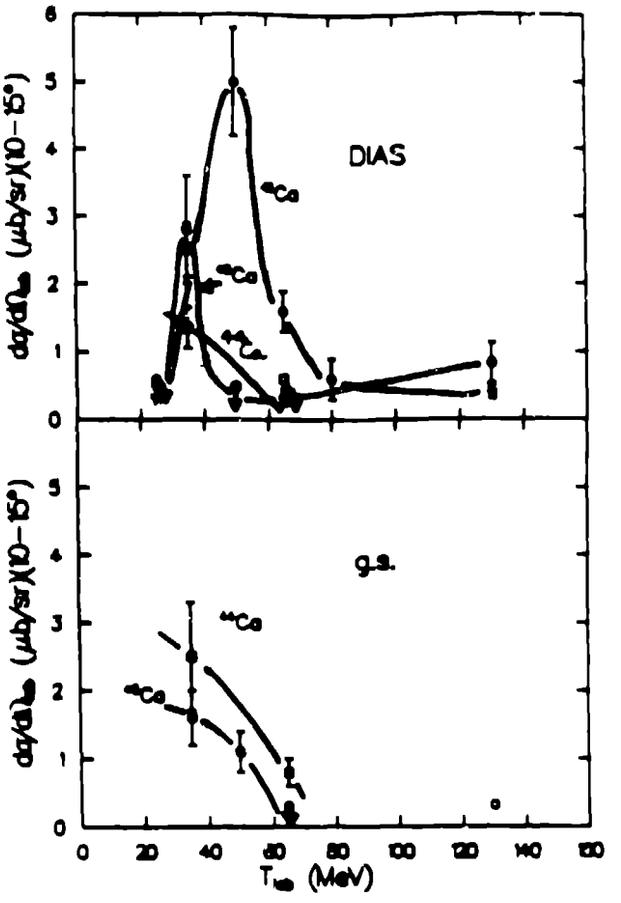

Fig. 29. Preliminary data on the energy-dependence of DIAS and g.s. transitions on calcium isotopes from our most recent run (Exp. 1098). The data at 80 and 130 MeV are from Kaletka *et al.* (Ref. 31).

Ref. 26 and must be treated within a more realistic $f^{7/2}$ model as shown by Auerbach, Gibbs, Ginocchio, and Kaufmann (AGGK).[27]

In this model the cross section for DIAS transitions is given by an expression similar to that of Eq. (1), which for the $f^{7/2}$-shell and $T = n/2$ is

$$\frac{d\sigma^{DIAS}}{d\Omega}(\theta) = \frac{n(n-1)}{2}|\tilde{A}(\theta) + X\tilde{B}(\theta)|^2 \quad , \tag{2}$$

where $X = (5-n)/|3(n-1)|$ with n being the number of valence nucleons. For the g.s. transition the analogous expression is,

$$\frac{d\sigma^{g.s.}}{d\Omega}(\theta) = \frac{n(n-1)}{2}|Y\tilde{B}(\theta)|^2 \quad , \tag{3}$$

where $Y = 4/|9(n-1)|\sqrt{(n-2)(10-n)}$.

Table II.

Q-values for various DCX reactions

Target	$Q_{g.s.}(MeV)$	$Q_{DIAS}(MeV)$	$E_x^{DIAS}(MeV)$
^{46}Ti	-13.64	-13.64	0.
^{50}Ti	-0.6	-13.22	13.06
^{50}Cr	-13.44	-14.83	1.39
^{54}Fe	-15.93	-15.90	0.
^{42}Ca	-12.40	-12.40	0.
^{44}Ca	-2.90	-12.33	9.44
^{48}Ca	5.29	-11.84	17.13

The resulting cross-section expressions are shown in Table III. For the purposes of the phenomological analysis here, I will work with the seniority model but apply corrections to these nuclei based upon the ratio between seniority and the full shell-model results of the reaction-model calculations in Ref. 27.

Table III.

Seniority Model Cross Sections from AGGK (Ref. 21)

	$d\sigma/d\Omega$	
Target	DIAS	g.s.
$^{42}Ca,^{54}Fe$	$\|A+B\|^2$	——
$^{44}Ca,^{52}Cr$	$6\|A+.11B\|^2$	$1.58B^2$
$^{46}Ca,^{50}Ti$	$15\|A-.07B\|^2$	$1.94B^2$
^{48}Ca	$28\|A-.14B\|^2$	$1.36B^2$
$^{46}Ti,^{50}Cr$	$\|A+1.47B\|^2$	——
$^{48}Ti,^{52}Cr$	$6\|A+.17B\|^2$	$2.3B^2$

(Note: $^{44}Ca(g.s.)/^{48}Ca(g.s.) = 1.16$)

The results of this phenomological approach are shown in Table IV. For 35 MeV I have fit the $^{42,44,48}Ca$ DIAS cross sections while for 65 MeV I have fit the $^{42,48}Ca$ DIAS

and the ^{44}Ca g.s. cross sections. For those nuclei where appropriate, the full shell model result is given first with the simpler pure seniority result in parenthesis below.

Table IV.

Seniority Model Fits (Preliminary Data)*

35 MeV		25 deg		40 deg		70 deg	
		data	AB†	data	AB†	data	AB†
DIAS	^{42}Ca	2.3±.5	2.22	1.9±.3	1.87	.4±.1	.38
DIAS	^{44}Ca	1.1±.3	1.12	1.1±.3	.96	.16±.04	.17
DIAS	^{50}Ti	1.6±.4	1.53	1.4±.3	1.32	.7±.2	.82
DIAS	^{48}Ca	2.7±.9	2.76	2.4±.7	2.36	2.2±.5	2.06
DIAS	^{46}Ti	2.5±.6	2.24 (4.37)	2.1±.40	1.86 (3.68)	.5±.1	.45 (.90)
DIAS	^{54}Fe	1.1±.3	2.22	.7±.2	1.87	<.07	.38
g.s.	^{44}Ca	—	1.42 (2.76)	—	1.15 (2.24)	—	.35 (.81)
g.s.	^{50}Ti	—	1.26 (3.21)	—	1.00 (2.69)	—	.37 (.97)
g.s.	^{48}Ca	1.6±.4	.91 (2.30)	—	.70 (1.98)	—	.17 (.69)

65 MeV		15 deg	
		data	AB†
DIAS	^{42}Ca	1.6±0.3	1.39
DIAS	^{44}Ca	<.6	0.73
DIAS	^{48}Ca	0.34±0.11	0.35
g.s.	^{44}Ca	0.8±0.2	.93 (1.37)
g.s.	^{48}Ca	<.3	.43 (1.18)

* For the 35 MeV $^{42,44,48}Ca$ the DIAS cross sections are fit; at 64 MeV the $^{42,48}Ca$ DIAS and the ^{44}Ca g.s. cross sections are fit.

† The AB numbers in parenthesis are the pure seniority results and those not in parenthesis are extended-seniority results obtained by scaling according to the 35 MeV/40 degree ratios of the AGGK paper[27]. (These are used even at 65 MeV.)

For 35 MeV at all three angles the agreement is excellent with the exception of ^{54}Fe. However, since this model neglects nuclear size differences and ^{54}Fe is substantially larger than the other nuclei, this may be such an effect. The angular distribution for

^{54}Fe (Fig. 26) is also much sharper. For 65 MeV, where we only have data at 15°, the agreement is also quite good except for the ^{48}Ca g.s. transition data which is anomolously small. Since the Q-values for the ^{48}Ca and ^{44}Ca g.s. transitions differ by about 7 MeV it is possible that at the edge of a rather sharp feature this difference may cause a shift that creates such a ratio. The small ^{48}Ca g.s. cross section appears to be the anomalous one since an attempt to include it in the fit rather than the ^{44}Ca g.s. makes the ^{43}Ca DIAS prediction much worse.

In summary the phenomological AB model appears to give an excellent description of the data with a few exceptions which may have simple explanations. With the success of the AB approach we can now begin to isolate the B strength which we associate with shorter-range correlations or perhaps with more exotic DCX mechanisms.

VI. SUMMARY AND CONCLUSIONS

We now believe that low-energy pion DCX is a significant new tool for studying nucleon-nucleon correlations in nuclei. The large cross sections, the isotopic ratios, and the different angular distributions for DCX on $f^{7/2}$-shell nuclei are understood in terms of a two-amplitude model which separates long and short-range correlation effects. The shell-model correlations of the nucleons involved is essential to explain these features of the data. The newest data on the energy dependence of both DIAS and g.s. transitions can still be understood in terms of a phenomological two-amplitude picture. We hope that the features of the data, especially the dramatic peaking near 50 MeV will constrain the theoretical models enough to determine whether additional correlations or new mechanisms must be involved.

I wish to thank the members of our collaboration, especially H. Baer, E. Piasetzky, and Z. Weinfeld, and also N. Auerbach, M. Blezynski, W. Gibbs, J. Ginocchio, R. Glauber, W. Kaufmann, and E. Siciliano for many useful discussions.

REFERENCES

1. D. Ashery *et al.*, Phys. Rev. C23, 2173 (1981); and I. Navon *et al.*, Phys. Rev. C28, 2548 (1983).

2. F. Irom, *et al.*, Phys. Rev. Lett. 55, 1862 (1985).

3. M. D. Cooper *et al.*, Phys. Rev. Lett. 52, 1100 (1984).

4. M. D. Cooper *et al.*, Progress at LAMPF, Los Alamos Report #LA-10429-PR, p. 47 (1984).

5. A. Doron *et al.*, Phys. Rev. C26, 189 (1983).

6. J. L. Ullmann *et al.*, Phys. Rev. C33, 2092 (1986).

7. M. J. Leitch *et al.*, Phys. Rev. C33, 278 (1986).

8. L. E. Ussery *et al.*, Phys. Rev. C38, 2761 (1988).

9. E. R. Siciliano *et al.*, Phys. Rev. C34, 267 (1986).

10. I. Navon *et al.*, Phys. Rev. Lett. 52, 105 (1984).

11. M. J. Leitch *et al.*, Phys. Rev. Lett. 54, 1482 (1985).

12. G. A. Miller, Phys. Rev. Lett. 53, 2008 (1984).

13. T. Karapiperis and M. Kobayashi, Phys. Rev. Lett. 54, 1230 (1985).

14. W. R. Gibbs *et al.*, LAMPF Workshop on Pion Double Charge Exchange, 1985, Los Alamos National Laboratory report LA-10550-C (eds. H. W. Baer and M. J. Leitch) p. 90ff.

15. M. Blezynski and R. J. Glauber, Phys. Rev. C36, 681 (1987).

16. A. Altman *et al.*, Phys. Rev. Lett. 55, 1273 (1985).

17. T. Anderl, Ph.D. thesis, "Mass- and Energy-Dependence of (π^+, π^-) Double Isobaric Analog Transitions at Low Energies," 1987, Universität at Bonn (unpublished).

18. M. J. Leitch *et al.*, Phys. Rev. C39, 2356 (1989).

19. J. A. Faucett *et al.*, Phys. Rev. C35, 1570 (1987).

20. P. A. Seidl *et al.*, Phys. Rev. C30, 978 (1984).

21. DCX data compilation by R. Gilman, Ph.D. Dissertation, "Systematics of Pion Double Charge Exchange," University of Pennsylvania, 1985 (Los Alamos report LA-10524-T).

22. W. R. Gibbs and W. B. Kaufmann, private communication.

23. K. Nakai *et al.*, Phys. Rev. Lett 44, 1446 (1980).

24. H. W. Baer *et al.*, Phys. Rev. C35, 1425 (1987).

25. Z. Weinfeld *et al.*, Phys. Rev. C37, 902 (1988).

26. N Auerbach, W. R. Gibbs, and E. Piasetsky, Phys. Rev. Lett. 59, 1076 (1987).

27. N. Auerbach, W. R. Gibbs, J. N. Ginocchio, and W. B. Kaufmann, Phys. Rev. C38, 1277 (1986).

28. Z. Weinfeld *et al.*, "Angular Distributions of Pion Induced Transitions to Double-Isobaric-Analog States on $f_{7/2}$ Nuclei at 35 MeV," submitted to Phys. Lett.

29. E. Bleszynski, M. Bleszynski, and R. J. Glauber, Phys. Rev. Lett. 60, 1483 (1988).

30. B. Levi, Physics Today, March 1988, p. 21.

31. M. Kaletka, Ph.D. Thesis, Northwestern Univ., "Core Excitation Effects in Pion Double Charge Exchange," Los Alamos National Laboratory Report LA-9947-T (1984), M. Kaletka *et al.*, Phys. Lett. B192, 336 (1987), and K. K. Seth *et al.*, Nucl. Phys. A478, 591c (1988).